



Phase transformations in a Cu–Zr–Al metallic glass

Qi Cheng^{a,b}, Xiaoliang Han^c, Ivan Kaban^c, Ivan Soldatov^d, Wei Hua Wang^{a,b,e},
Yong Hao Sun^{a,b,e}, Jiri Orava^{c,*}

^a Institute of Physics, Chinese Academy of Sciences, Beijing 100190, China

^b Center of Materials Science and Optoelectronics Engineering, University of Chinese Academy of Sciences, Beijing 100049, China

^c IFW Dresden, Institute for Complex Materials, Helmholtzstraße 20, Dresden 010 69, Germany

^d IFW Dresden, Institute for Metallic Materials, Helmholtzstraße 20, Dresden 010 69, Germany

^e Songshan Lake Materials Laboratory, Dongguan, Guangdong 523808, China

ARTICLE INFO

Article history:

Received 4 February 2020

Revised 11 March 2020

Accepted 11 March 2020

Keywords:

Fast scanning calorimetry

Crystallization

Phase transformations

Metallic glass

ABSTRACT

A combination of conventional calorimetry, ultra-fast scanning calorimetry and resistive heating gives access to heating rates exceeding 6 orders of magnitude allowing to probe crystallization kinetics and mechanisms in a Cu–Zr–Al metallic glass. Continuous-heating-transformation and double-peak time-temperature-transformation diagrams are constructed and related to the formation of glass–crystal composites with enhanced ductility. The metastable B2–CuZr phase becomes dominantly formed at a heating rate of $\sim 10^2$ K s⁻¹ and higher. A critical heating rate to bypass crystallization is $\sim 10,000$ K s⁻¹. For isothermal annealing at >850 K, only one crystallization event is detected; for lower temperatures, a complex two-step transformation occurs.

© 2020 Acta Materialia Inc. Published by Elsevier Ltd. All rights reserved.

Phase transformations of glass-forming alloys are of fundamental interest to understand the kinetic and thermodynamic propensity to glass formation [1,2], and to produce technologically important glasses and glass–crystal composites. Oxide-based glass-ceramics have a wide range of applications including biocomponents [3]. Metallic-glass-(MG)-crystal composites have important functional properties [4], and have also attracted great attention as structural biomaterials [5] because of their biocompatibility and mechanical performance. The formation of MG–crystal composites, having ductile crystalline phase(s), has been found to be very efficient in enhancing plasticity (ductility) and toughness of otherwise brittle MGs [6–8]. The final composite microstructure is better controlled on heating a glass rather than on cooling a liquid. Crystallization mechanism can easily be tuned by controlling heating rate, Φ , and composites with uniformly dispersed crystals of defined sizes in the glassy matrix are desired [9–13].

The Cu–Zr-based family of MGs is the prototype to make the composites. The equimolar compound is a good glass former [14]. Alloying Cu–Zr MG with Al can further improve the glass-forming ability [15], and glassy rods of ~ 3 –5-mm in a diameter, with the respective critical cooling rates ~ 110 – 40 K s⁻¹ estimated by the assumption given in Ref. [16], have been reported [8,17–19]. Here,

the focus is on Cu_{47.5}Zr_{47.5}Al_{5.0} glass (at.%). The supercooled liquid is stable over a relatively wide temperature range (the thermal stability, expressed as $\Delta T_x = T_x - T_g$, is ~ 50 – 80 K at conventional Φ [17,20]; T_g – glass-transition temperature, T_x – crystallization onset temperature); the glasses have good mechanical properties [21] and physico-chemical properties are known [22–24]. In particular, MG–crystal composites can be made toward improved tensile ductility by introducing the metastable B2-type CuZr phase into the glass [7,8,11]. The B2–CuZr stable equilibrium temperature is above 900 K, but it can also form at lower temperatures when glasses are heated ‘sufficiently’ fast. In fact, when Φ is high enough, for example, 500 K min⁻¹ for Zr₅₀Cu₄₀Al₁₀ [13] and ~ 232 K s⁻¹ for Cu₄₄Zr₄₄Al₈Hf₂Co₂ glass [10], the B2–CuZr is dominantly formed.

The thermodynamic and kinetic properties, relevant for the ductile-composite formation, have been explored by using fast-resistive [11,25], induction [10] and capacitance-discharge heating [26,27]. Nevertheless, time-temperature-transformation (TTT) diagrams have not been obtained because the isothermal holding temperature is difficult to control. Kosiba et al. [9] attempted to measure continuous-heating-transformation (CHT) diagram by inductive-coil-induced heating. However, heating between room temperature– T_g – T_x is non-linear, especially for low Φ , therefore it is difficult to transpose T_g and T_x on the same heating curve, and Φ was limited to ≤ 150 K s⁻¹. Because of the need for high Φ , the

* Corresponding author.

E-mail addresses: ysun58@iphy.ac.cn (Y.H. Sun), j.orava@ifw-dresden.de (J. Orava).

quantitative assessment of TTT and CHT diagrams is impossible by conventional calorimetry.

Fast-heating differential scanning calorimetry (FDSC) has typically been applied to study polymers because the upper-temperature limit is ~ 790 K for the previous generation. Recently, the technique has been widespread and applied to metallic compounds to study crystallization of low-melting single metals (Bi [28]), $\text{Pb}_{90}\text{Bi}_{10}$ [29], rare-earth-based [30], Au-based [31], and to Al-based [32] MGs. A new generation of FDSC instruments – Flash DSC 2+, developed by Mettler Toledo, with a high-temperature UFH 1 sensor – enables measurements with Φ up to $60,000 \text{ K s}^{-1}$ and has a theoretical upper-temperature limit at around 1270 K, and these provide direct access for CHT and TTT diagrams determination of $\text{Cu}_{47.5}\text{Zr}_{47.5}\text{Al}_{5.0}$ glass. The new FDSC 2+ has mainly been used to study low-melting Au-based MGs [1] for which the influence of the liquid's thermal history on crystallization kinetics can readily be studied. So far, for example, Lee et al. [33] and Miao et al. [34] have presented FDSC studies of a thin-film Cu-Zr-based MGs in a wide range of heating rates and up to high temperatures by using a custom-made nano-calorimeter.

In this work, FDSC measurements of the $\text{Cu}_{47.5}\text{Zr}_{47.5}\text{Al}_{5.0}$ ribbon, using the FDSC 2+ instrument, are performed and complemented by conventional DSC and rapid-resistive heating. New CHT and TTT diagrams for the crystallization of $\text{Cu}_{47.5}\text{Zr}_{47.5}\text{Al}_{5.0}$ glass are obtained and they help to understand the transformation kinetics relevant for the formation of ductile glass–crystal composites.

Sample preparation. The $\text{Cu}_{47.5}\text{Zr}_{47.5}\text{Al}_{5.0}$ ribbon, $\approx 30 \mu\text{m}$ thick and ~ 2 mm wide, was spun from a master-alloy melt ($T = 1320$ K) on a Cu wheel rotating at 29 m s^{-1} . The ribbon amorphicity was confirmed by x-ray diffraction measurements of both sides using a Malvern Panalytical PW3040/60 X'PertPro equipped with a Co $K\alpha$ source. **Calorimetry.** The as-cast ribbons were cut into small rectangular-like pieces of an approximate mass of $1 \mu\text{g}$ for FDSC. The sample-support temperature of FDSC was set to $T = 300$ K, and the heating chamber was purged with an Ar-gas flow rate of $80 \text{ cm}^3 \text{ min}^{-1}$. The temperature calibration, using the melting of standard metals, and thermal lag estimation were done as described in Refs. [35,36]. A PerkinElmer DSC 8500, purged with an Ar-gas flow of $20 \text{ cm}^3 \text{ min}^{-1}$, was used for conventional calorimetric measurements; the sample mass was ~ 15 mg. **Resistive heating.** A rapid-resistive-heating setup is detailed in Ref. [37] – see Fig. 4 part a and b. A 3-cm long piece of the ribbon was annealed via Joule heating in a vacuum of $\sim 10^{-4}$ mbar at $\Phi = 10^3\text{--}10^4 \text{ K s}^{-1}$ using a Delta Elektronika SM 52–32 DC power supply, while resistance was monitored. Temperature was read from the ribbon center using an IMPAC pyrometer IGA 320/23-LO (a spot diameter < 1.5 mm) with a temporal resolution of 2×10^{-3} s. The pyrometer was calibrated on the known melting temperature $T_m = 1148$ K of the glass; measured independently by using a high-temperature Netzsch DSC 4040 calorimeter (Fig. S1).

Thermal contact between a sample and an FDSC sensor represents one of the most critical and variable parameters influencing a thermal lag and calorimetric measurements. For this reason, a thermal-contacting method, also applied for FDSC of polymers [38], has been used, as schematically shown in Fig. 1. A double thermal-contacting period is introduced at 573 and 673 K, both being below $T_g = 693$ K at $\Phi = 40 \text{ K min}^{-1}$, with annealing time of 60 s, before FDSC measurement. This annealing period necessitates measurement reproducibility. Without it, good thermal contact cannot be reproduced, and sample jumping off the sensor, characteristic for metallic samples, can be observed [38]. The short thermal-contacting period has pronounced annealing effect on the sub- T_g relaxation region of the as-cast glass (Fig. S2) represented by the enthalpy of relaxation changing from $\sim 0.7\text{--}1.0 \text{ kJ mol}^{-1}$ for the as-cast to zero for the thermally-contacted glass. There is no

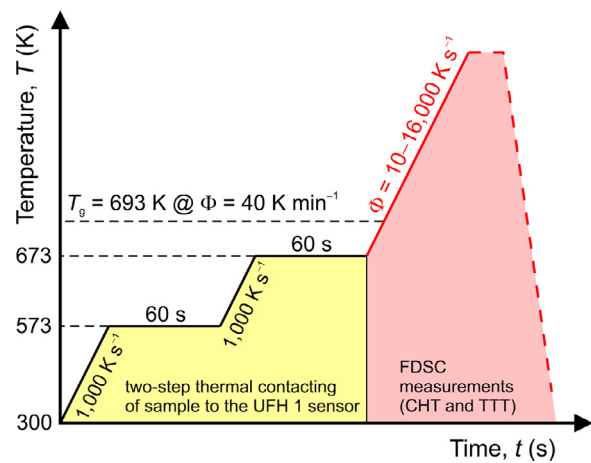


Fig. 1. Schematic of a heating profile used for continuous-heating-transformation (CHT) and time-temperature-transformation (TTT) phase diagrams measurements. A two-step sample-sensor thermal-contacting period, fast annealing of the as-cast glass at the temperatures below the glass-transition temperature T_g , precedes the FDSC phase-transformation measurements (Φ – heating rate).

change in T_g and T_{x1} between the as-cast and the fast-annealed glass (Fig. S2). Similarly, there is no difference between T_g and T_{x1} when the glass is well-annealed even at $1.05T_g$ for 2 min [39].

Representative isokinetic calorimetric traces (Fig. 2a) show T_g and the onset of the primary crystallization, T_{x1} . With the present sensor used, no signal can be observed at ≥ 1000 K (not shown). Above this temperature, probably a reaction between the glass and the sensor occurs, and stress conditions change, resulting in the sensor breaking. This limits T_x -readings for FDSC to $\Phi \leq 2900 \text{ K s}^{-1}$, and also T_m cannot be accessed. To overcome the limitation, the resistive heating is applied to determine T_{x1} on faster heating. Characteristic temporal evolution of the resistance and temperature is shown in Fig. 2b at $\sim 7000 \text{ K s}^{-1}$ – T_{x1} and t_{x1} are read as the resistance drop accompanied by the recalcination event. A linear heating rate is calculated to match T_{x1} and t_{x1} when they are transposed on the CHT plot. The origin of the weak drop in resistance, preceding T_{x1} , still remains somewhat unclear. Its temperature lies close to T_g (Fig. 2c). For a $\text{Cu}_x\text{Zr}_{84-x}\text{Al}_8\text{Ag}_8$ MG and conventional Φ , a resistivity drop was associated with T_g [40]. A weak change in resistivity below T_g was also observed for a Ni-Pd-P glass, and though no sub- T_g relaxation in calorimetry was detected, the change was clearly associated with structural changes in the glass [41]. The as-cast glass $\text{Cu}_{47.5}\text{Zr}_{47.5}\text{Al}_{5.0}$ relaxes over a wide temperature range from 490 K up to T_g (sub- T_g exotherm in Fig. S2), and such a complex relaxation overlapping with the glass transition can be the underlying process manifested by the weak resistance drop.

The measured T_g and T_{x1} as a function of Φ are shown in Fig. 2c – represented as a CHT diagram. For the low heating rates, $\Phi < \sim 1.6666 \text{ K s}^{-1}$ (100 K min^{-1}), corresponding to the range of conventional DSC, the thermal stability of the supercooled liquid, ΔT_x , is 74 K. For the intermediate heating rates, $\sim 1 < \Phi \leq 2900 \text{ K s}^{-1}$, corresponding to the range of FDSC, the thermal stability is 74–110 K. The region of the existence of supercooled liquid widens up to $\Delta T_x = 171$ K at $10,000 \text{ K s}^{-1}$, which is probed by the resistive heating. For the low heating rates, the primary crystallization can be characterized by the formation of $\text{Cu}_{10}\text{Zr}_7$ and CuZr_2 as the major phases [42,43], which then, on continuous heating, react endothermically to form B2 CuZr [33,44] at around $T_{x2} = 980$ K (shown on the CHT plot and obtained by conventional high-temperature calorimetry – Fig. S1). The endothermic reaction cannot be seen in the present FDSC traces, unlike for thin-film

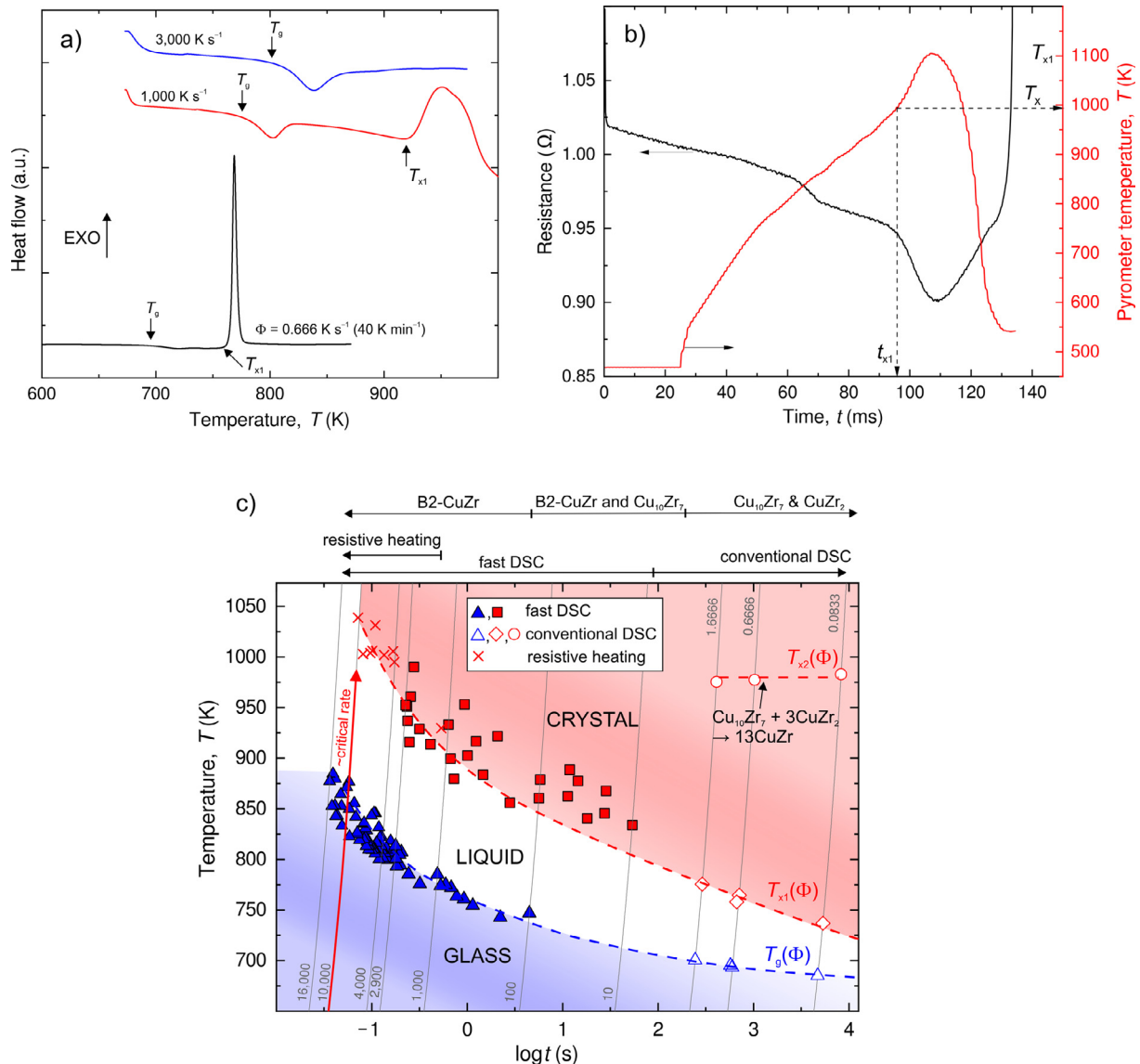


Fig. 2. (a) Isochronic calorimetric traces showing the glass-transition temperature, T_g , and the temperature of the primary crystallization onset, T_{x1} , for conventional ($\Phi = 0.666 \text{ K s}^{-1}$) and for fast DSC ($\Phi = 1000$ and 3000 K s^{-1}). (b) Temporal evolution of $\text{Cu}_{47.5}\text{Zr}_{47.5}\text{Al}_{5.0}$ ribbon resistance (left-hand abscissa) and pyrometer temperature reading (right-hand abscissa) during fast Joule heating at $\Phi \sim 7000 \text{ K s}^{-1}$. The crystallization time, t_{x1} , and the onset temperature of the primary crystallization, T_{x1} , can readily be detected as the resistance drop and the recalescence event on the corresponding time-dependent plots. (c) A continuous-heating-transformation diagram for crystallization of $\text{Cu}_{47.5}\text{Zr}_{47.5}\text{Al}_{5.0}$ glass. The heating-rate-dependent evolution of T_g (triangles) and T_x (diamonds, squares, circles and crosses) were measured by conventional DSC, $\Phi \leq 1.6666 \text{ K s}^{-1}$ (open symbols), fast DSC, $10 \leq \Phi \leq 16,000 \text{ K s}^{-1}$ (full symbols) and resistive heating, $\Phi > 1000 \text{ K s}^{-1}$ (crosses). The isokinetic curves are labeled with the corresponding heating rates in K s^{-1} . The upper part highlights the ranges of Φ for which the characteristic (dominant) products of primary crystallization may exist. The dashed lines are to guide the eyes only.

$\text{Cu}_{50}\text{Zr}_{50}$ [33]; the reaction temperature is just at the temperature detection limit. As noted by Kalay et al. [43,44] for isokinetic heating at 10 K min^{-1} : i) the B2 phase can already form during the primary crystallization, then dissolves and re-precipitates later on heating; and ii) $\text{Cu}_{10}\text{Zr}_7$ co-exists with the B2 phase until melting is reached. Above a critical heating rate of about 250 K s^{-1} [11], the polymorphic crystallization of the B2-CuZr phase becomes the dominant mechanism in $\text{Cu}_{47.5}\text{Zr}_{47.5}\text{Al}_{5.0}$, and ductile glass-crystal composites can be formed [7,37].

A trend in the temperature-dependent activation energy for crystallization, $E_a(T)$, represented by the Kissinger plot [45] and shown as the red dashed line by taking only the lowest T_{x1} representing the ‘best thermal contact’ for a given Φ , has a non-Arrhenius dependence (Fig. 3). The curvature to some extent reflects the intermediate-to-strong kinetic fragility character of the

liquid [33,46], i.e., the underlying temperature-dependent viscosity for which experimental data are unavailable. Because it is the onset temperature, the relationship between mobility and the curvature is not as straightforward as, for example, for relating a DSC peak maximum to crystallization kinetics [46]. A curvature in $E_a(T)$, by considering the DSC peak maximum, has also been observed by nano-calorimetry for thin-film $\text{Cu}_{50}\text{Zr}_{50}$ [33] and related to its kinetic fragility ~ 50 [47] via a growth-limited model. An Arrhenius fit to the conventional DSC data gives $E_a = 354 \text{ kJ mol}^{-1}$.

A critical heating rate to overcome crystallization on heating is around $10,000 \text{ K s}^{-1}$ (Fig. 2c). For faster rates, the glass goes directly into the high-temperature liquid, and the ribbon collapses under resistive heating (not shown in Fig. 2b). The critical heating rate is ~ 2 orders of magnitude greater than a critical cooling rate, $\sim 100 \text{ K s}^{-1}$, for this glass. The asymmetry is understood in terms of

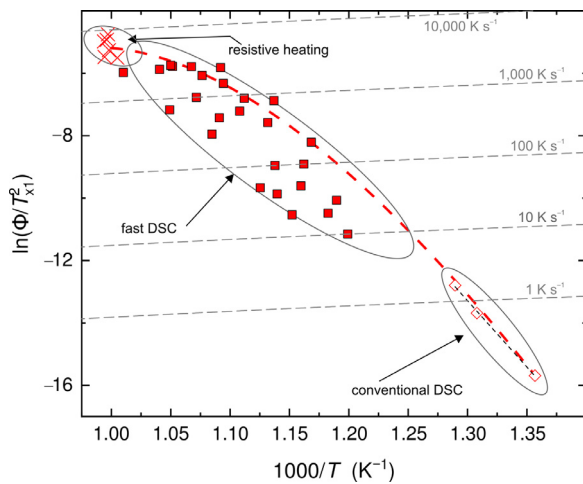


Fig. 3. A Kissinger plot for crystallization of $\text{Cu}_{47.5}\text{Zr}_{47.5}\text{Al}_{5.0}$. The evolution of the onset of crystallization T_{x1} with heating rate Φ (K s^{-1}) is plotted. The red dashed line shows a trend in the temperature-dependent activation energy for crystallization over the entire measured range by considering the lowest values of T_{x1} at a given Φ only. An Arrhenius-type fit to the conventional DSC data is shown by the black dashed line. The horizontal dashed lines show the corresponding heating rate. (For interpretation of the references to color in this figure legend, the reader is referred to the web version of this article.)

a higher density of the frozen-in nuclei in a glass than in a liquid [1]. Johnson et al. [26] calculated a critical heating rate of $\sim 10^4 \text{ K s}^{-1}$ for Zr-based MGs having a typical critical casting diameter of a few millimeters. Kosiba [48] estimated a critical heating rate of about 10^3 K s^{-1} for $\text{Cu}_{46}\text{Zr}_{46}\text{Al}_8$ glass.

For polymorphic crystal growth, the temperature at which the crystal-growth rate reaches its maximum is found at $T_{\text{max}} = (1.48 \pm 0.15)T_g$ [49], giving $T_{\text{max}} \approx 1025 \text{ K}$ ($0.89T_m$), which coincides with the CHT nose at $\sim 950 \text{ K}$. Computer simulations show $T_{\text{max}} = 1000 \text{ K}$ ($0.87T_m$) for the B2 phase in the supercooled liquid $\text{Cu}_{47.5}\text{Zr}_{47.5}\text{Al}_{5.0}$ [50]. This temperature conforms to the CHT nose, being thus growth-dominated, and also to growth-controlled mechanism found for $\text{Cu}_{50}\text{Zr}_{50}$ [33].

Isothermal fast DSC traces (Fig. 4a), preceded with heating at $10,000 \text{ K s}^{-1}$, are used to construct a TTT diagram (Fig. 4b). The

diagram has two noses located at $\sim 850 \text{ K}$ ($0.74T_m$) and at $\sim 950 \text{ K}$ ($0.83T_m$). For $T \leq 850 \text{ K}$ ($0.73T_m$), primary T_{x1} and also secondary T_{x2} transformations are observed between $800\text{--}843 \text{ K}$; the annealing time is limited to 60 s (inset in Fig. 4a). Cullinan et al. [51] showed by x-ray diffraction that isothermal crystallization of $\text{Cu}_{50}\text{Zr}_{50}$ glass at 671 K ($0.67T_m$), a temperature at which the B2 should not be stable, is as follows: the primary phase is $\text{Cu}_{10}\text{Zr}_7$, which is then followed by CuZr_2 precipitation on continued annealing and this phase templates the metastable B2 CuZr growth. Although we do not have direct evidence about phase evolution, we speculate that a similar mechanism may prevail for isothermal annealing of $\text{Cu}_{47.5}\text{Zr}_{47.5}\text{Al}_{5.0}$ because the homologous temperatures are close to each other. However, without detailed microstructural analysis, we are not able to assign the T_{x2} to a specific phase formation. Some form of the $\text{Cu}_{10}\text{Zr}_7/\text{CuZr}_2 \rightarrow \text{B2-CuZr}$ crystallization sequence is the most accepted one for both isokinetic heating at conventional heating rates and isothermal annealing at temperatures just above T_g [33,37]. Other intermetallic phases can form, too [44].

For $T > 850 \text{ K}$ only one crystallization event is observed. The temperature of the second nose falls into the region of the highest crystal-growth rate of the B2 phase in the liquid. For $\text{Cu}_{50}\text{Zr}_{50}$, the region spans between $(0.74\text{--}0.90)T_m$ with weakly-temperature dependent growth [47], which may give not so distinctly sharp nose on TTT diagram as shown, for example, for some fast-crystal-growth rate metallic liquids [52].

To conclude, new CHT and TTT diagrams of the supercooled liquid $\text{Cu}_{47.5}\text{Zr}_{47.5}\text{Al}_{5.0}$ up to $\sim 1000 \text{ K}$ were obtained by using the combination of conventional DSC, fast DSC and resistive heating with Φ spanning over 6 orders of magnitude from $10^{-2}\text{--}10^4 \text{ K s}^{-1}$. Both CHT and TTT diagrams could be constructed highlighting the crystallization mechanism of the glass, being growth-rate controlled for temperatures higher than 850 K , and relate to the formation of glass-crystal composites with enhanced ductility. The ductility is provided by the B2-CuZr phase. For heating rates lower than $\sim 10 \text{ K s}^{-1}$, $\text{Cu}_{10}\text{Zr}_7$ and CuZr_2 phases form during the primary crystallization. With faster heating, 10^2 K s^{-1} and higher, the B2 phase becomes dominantly formed. A critical heating rate to bypass crystallization is $\sim 10,000 \text{ K s}^{-1}$. A double-peak TTT diagram was measured by fast DSC. For isothermal annealing at $T > 850 \text{ K}$, only one crystallization event was detected probably suggesting the B2 CuZr

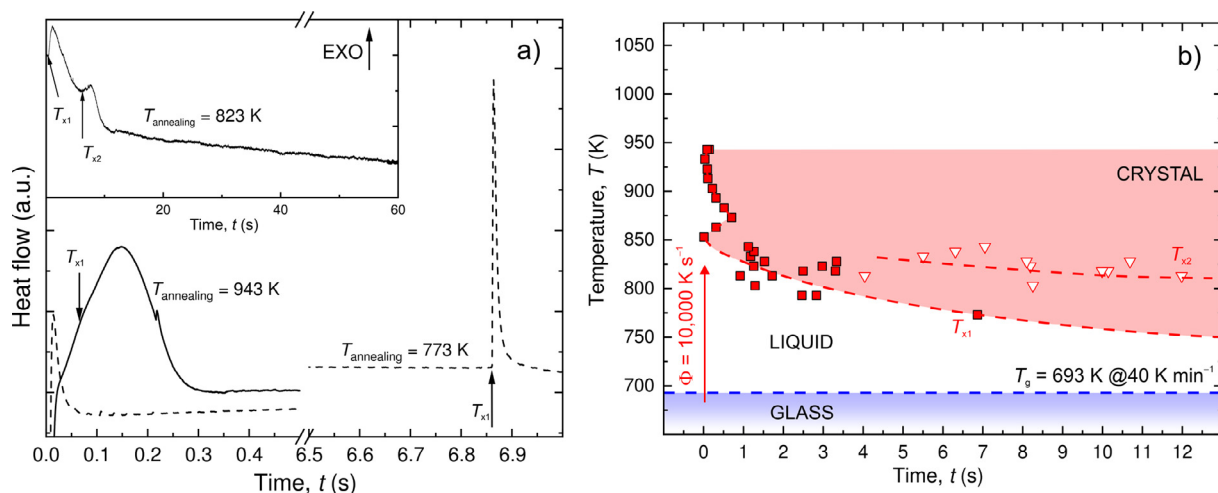


Fig. 4. (a) Fast DSC traces for the lowest (773 K) and the highest (943 K) measured annealing temperatures. The inset shows an example of isothermal annealing with two crystallization events at 823 K . The maximum annealing time is 60 s . (b) A double-peak time-temperature-transformation diagram for crystallization of $\text{Cu}_{47.5}\text{Zr}_{47.5}\text{Al}_{5.0}$ glass. The temperatures of the primary (squares), T_{x1} , and the secondary (triangles), T_{x2} , crystallization, when applicable below $T \leq 843 \text{ K}$, are shown by the symbols. The dashed lines are to guide the eyes only.

formation as the dominant phase, and that the nose is growth-rate dominated. For isothermal annealing at $T < 850$ K, a complex two-step transformation occurs.

Declaration of Competing Interest

The authors declare that they have no known competing financial interests or personal relationships that could have appeared to influence the work reported in this paper.

Acknowledgments

JO and IK thank the German Research Foundation DFG, Contract No. Ka-3209/9-1, and YHS thank the National Natural Science Foundation of China (51971238), for funding. JO and YHS acknowledge the financial support of the promising Young scientists award from the Center for International Collaboration (IOPCIC), the Institute of Physics, the Chinese Academy of Sciences. We are very grateful to H. Siegel, S. Ziller, B. Bartusch and B. Opitz (IFW Dresden) for technical support.

Supplementary materials

Supplementary material associated with this article can be found, in the online version, at doi:10.1016/j.scriptamat.2020.03.028.

References

- [1] J.E.K. Schawe, J.F. Löffler, *Nat. Commun.* 10 (2019) 1337.
- [2] K.F. Kelton, A.L. Greer, *Nucleation in Condensed Matter: Applications in Materials and Biology*, Elsevier, Oxford, 2010.
- [3] E.D. Zanotto, *Am. Ceram. Soc. Bull.* 89 (2010) 19.
- [4] J.M. Silveyra, E. Ferrara, D.L. Huber, T.C. Monson, *Science* 362 (2018) eaa0195.
- [5] H.F. Li, Y.F. Zheng, *Acta Biomater.* 36 (2016) 1.
- [6] S. Pauly, G. Liu, G. Wang, U. Kühn, N. Mattern, J. Eckert, *Acta Mater.* 57 (2009) 5445.
- [7] S. Pauly, S. Gorantla, G. Wang, U. Kühn, J. Eckert, *Nat. Mater.* 9 (2010) 473.
- [8] Y. Wu, H. Wang, H.W. Wu, Z.Y. Zhang, X.D. Hui, G.L. Chen, D. Ma, X.L. Wang, Z.P. Lu, *Acta Mater.* 59 (2011) 2928.
- [9] K. Kosiba, S. Scudino, R. Kobold, U. Kühn, A.L. Greer, J. Eckert, S. Pauly, *Acta Mater.* 127 (2017) 416.
- [10] K. Kosiba, S. Pauly, *Sci. Rep.* 7 (2017) 2151.
- [11] I.V. Okulov, I.V. Soldatov, M.F. Sarmanova, I. Kaban, T. Gemming, K. Edström, J. Eckert, *Nat. Commun.* 6 (2015) 7932.
- [12] K.K. Song, X.L. Han, S. Pauly, Y.S. Qin, K. Kosiba, C.X. Peng, J.H. Gong, P.X. Chen, L. Wang, B. Sarac, S. Ketov, M. Mühlbacher, F. Spieckermann, I. Kaban, J. Eckert, *Mater. Des.* 139 (2018) 132.
- [13] S. Zhang, T. Ichitsubo, Y. Yokoyama, T. Yamamoto, E. Matsubara, A. Inoue, *Mater. Trans.* 50 (2009) 1340.
- [14] W.H. Wang, J.J. Lewandowski, A.L. Greer, *J. Mater. Res.* 20 (2005) 2307.
- [15] Q. An, K. Samwer, W.A. Goddard III, W.L. Johnson, A. Jaramillo-Botero, G. Garret, M.D. Demetriou, *J. Phys. Chem. Lett.* 3 (2012) 3143.
- [16] X.H. Lin, W.L. Johnson, *J. Appl. Phys.* 78 (1995) 6514.
- [17] P. Yu, H.Y. Bai, M.B. Tang, W.L. Wang, *J. Non-Cryst. Solids* 351 (2005) 1328.
- [18] H.B. Yu, W.H. Wang, H.Y. Bai, *Appl. Phys. Lett.* 96 (2010) 081902.
- [19] C.Y. Yu, X.J. Liu, G.P. Zheng, X.R. Niu, C.T. Liu, *J. Alloys Compd.* 627 (2015) 48.
- [20] S. Pauly, J. Das, N. Mattern, D.H. Kim, J. Eckert, *Intermetallics* 17 (2009) 453.
- [21] W.H. Wang, *Prog. Mater. Sci.* 57 (2012) 487.
- [22] G.J. Fan, M. Freels, H. Choo, P.K. Liaw, J.J.Z. Li, W.-K. Rhim, W.L. Johnson, P. Yu, W.H. Wang, *Appl. Phys. Lett.* 89 (2006) 241917.
- [23] W.H. Wang, C. Dong, C.H. Shek, *Mater. Sci. Eng. R* 44 (2004) 45.
- [24] W.H. Wang, *Prog. Mater. Sci.* 106 (2019) 100561.
- [25] S. Küchemann, G. Gibbins, J. Corkerton, E. Brug, J. Ruebsam, K. Samwer, *Phil. Mag.* 96 (2016) 454.
- [26] W.L. Johnson, G. Kaltenboeck, M.D. Demetriou, J.P. Schramm, X. Liu, K. Samwer, C.P. Kim, D.C. Hofmann, *Science* 332 (2011) 828.
- [27] S. Küchemann, K. Samwer, *Acta Mater.* 119 (2016) 119.
- [28] K. Xiao, J.J. Vlassak, *Thermochim. Acta* 603 (2015) 29.
- [29] J.H. Perepezko, T.W. Glendinning, J.-Q. Wang, *Thermochim. Acta* 603 (2015) 24.
- [30] B. Zhao, A.M. Rodrigues, K. Ding, H. Ma, G. Wu, Q. Zhai, Y. Gao, *Intermetallics* 116 (2020) 106653.
- [31] S. Pogatscher, D. Leutenegger, J.E.K. Schawe, P.J. Uggowitzer, J.F. Löffler, *Nat. Commun.* 7 (2016) 11113.
- [32] M. Gao, J.H. Perepezko, *Thermochim. Acta* 677 (2019) 91.
- [33] D. Lee, B. Zhao, E. Perim, H. Zhang, P. Gong, Y. Gao, Y. Liu, C. Toher, S. Curtarolo, J. Schroers, J.J. Vlassak, *Acta Mater.* 121 (2016) 68.
- [34] Y. Miao, R. Villarreal, A. Talapatra, R. Arróyave, J.J. Vlassak, *Acta Mater.* 182 (2020) 29.
- [35] E. Zhuravlev, C. Schick, *Thermochim. Acta* 505 (2010) 1.
- [36] E. Zhuravlev, C. Schick, *Thermochim. Acta* 505 (2010) 14.
- [37] J. Orava, I. Kaban, M. Benkocka, X. Han, I. Soldatov, A.L. Greer, *Thermochim. Acta* 677 (2019) 198.
- [38] J.E.K. Schawe, S. Pogatscher, *Material characterization by fast scanning calorimetry: practice and applications*, in: C. Schick, V. Mathot (Eds.), *Fast Scanning Calorimetry*, Springer, Switzerland, 2016, pp. 3–80.
- [39] W. Guo, R. Yamada, J. Saida, *Mater. Sci. Eng. A* 699 (2017) 81.
- [40] L.-F. Wang, X. Cui, Q.-D. Zhang, F.-Q. Zu, *Met. Mater. Int* 20 (2014) 669.
- [41] I. Kaban, K. Khalouk, F. Gasses, J.-G. Gasses, J. Bednarcik, O. Shuleshova, I. Okulov, T. Gemming, N. Mattern, J. Eckert, *J. Alloy. Compd.* 615 (2014) S208.
- [42] I. Kalay, M.J. Kramer, R.E. Napolitano, *Metal. Mater. Trans. A* 42A (2011) 1144.
- [43] I. Kalay, M.J. Kramer, R.E. Napolitano, *Metal. Mater. Trans. A* 46A (2015) 3356.
- [44] L. Treyachenko, Al-Cu-Zr (aluminium-copper-zirconium), in: G. Effenberg, S. Ilyenko (Eds.), *Landolt-Börnstein - Group IV Physical Chemistry 11A2 (Light Metal Systems Part 2)*, SpringerMaterials, Berlin, 2005, pp. 206–222.
- [45] H.E. Kissinger, *Anal. Chem.* 29 (1957) 1702.
- [46] J. Orava, A.L. Greer, *Thermochim. Acta* 603 (2015) 63.
- [47] Q. Wang, L.-M. Wang, M.Z. Ma, S. Binder, T. Volkman, D.M. Herlach, J.S. Wang, Q.G. Xue, Y.J. Tian, R.P. Liu, *Phys. Rev. B* 83 (2011) 014202.
- [48] K. Kosiba, *Flash-Annealing of Cu-Zr-Al-based bulk metallic glasses*, 2017 <https://nbn-resolving.org/urn:nbn:de:bsz:14-qucosa-222874>.
- [49] J. Orava, A.L. Greer, *J. Chem. Phys.* 140 (2014) 214504.
- [50] V. Kokotin, H. Hermann, J. Eckert, *J. Phys.: Condens. Matter* 23 (2011) 425403.
- [51] T. Cullinan, I. Kalay, E. Kalay, M. Kramer, R. Napolitano, *Metal. Mater. Trans. A* 46A (2015) 600.
- [52] J. Orava, A.L. Greer, *Acta Mater* 139 (2017) 226.